2. Upper boundary condition*

2.1 Introduction

Almost any models, so far, use ω (the vertical p-velocity)$=0$ or w (the vertical velocity)$=0$ as the upper boundary condition, the use of which causes reflection of wave energy as demonstrated by Lindzen *et al.*(1966). If we apply the condition, $\omega=0$, at the level $p=p_t$ ($\neq 0$), air particles are not allowed to cross the level $p=p_t$ from below to above it, which is not true in the real atmosphere, and thus causes wave reflections. This situation is not essentially changed at all even when p_t is replaced by 0, unless sub-grid-scale physical processes in the vertical direction are properly included parametrically in the model.

So far as the open boundary condition in the horizontal directions is concerned, several methods have been proposed (Wurtele *et al.*, 1971; Pearson, 1974; Beland and Warn, 1975; Orlanski, 1976, *etc.*). The method proposed by the above authors is essentially the implementation of Sommerfeld radiation condition. By estimating phase velocity in the normal direction to the boundary, say c, we may write Sommerfeld radiation condition as;

$$\frac{\partial \psi}{\partial t}+c\frac{\partial \psi}{\partial n}=0 \tag{2.1}$$

for a variable ψ, where n is the coordinate normal to the boundary. The authors mentioned above discuss various ways of applying Eq. (2.1) to the unbounded hyperbolic flows. Beland and Warn (1975) have derived a transient radiation condition for both Rossby and inertio-gravity waves.

As an upper boundary condition, one may think of using Eq. (2.1), replacing ψ by ω or w. However, this method, as is shown in the Appendix 2.2, turns out to be impractical, because the method causes instability, the growth rate of which is not small, especially in the low latitude regions.

In this paper, we describe, as an alternative method, a sponge layer model. In the sponge layer model, we include a sponge term in the thermodynamic equation, which is designed to cancel out erroneous effects caused by the inappropriate upper boundary condition, $\omega=0$, below the sponge layer. In another words, the sponge layer is designed so as to play an equivalent role to the radiation condition.

---

* This chapter is prepared by T. Tokioka.

Although the sponge term is a kind of generalization of a Newtonian cooling term, it is required to be highly dependent on modes, especially on frequency, and is also required to be a complex number. The real part of the sponge term has a damping effect as a Newtonian cooling term does, while the imaginary part modifies the vertical wavenumber of a disturbance in the sponge layer.

The basic formulation of the sponge layer model has already been presented in Chapter 4 of AM (1974). In section 2.2, a discrete form of vertical structure equation is derived. The effect of upper boundary condition is demonstrated in 2.3. A "sponge layer" is formulated in 2.4, where we describe one practical way of applying the sponge layer model to the global circulation model. Some test examples of the sponge layer model are presented in the Appendix 2.1, demonstrating that the model works well to the forcings with the wide range of Lamb's parameter, when only one mode is forced from below.

2.2 The vertical structure equation

Using the vertical index k shown in Fig. 1.2, the equations linearized with respect to perturbations on a resting isothermal basic state, may be written in a discrete model as

$$i\sigma\hat{u}_k - 2\Omega\sin\varphi\hat{v}_k + \frac{is}{a\cos\varphi}\hat{\phi}_k = 0 \tag{2.2}$$

$$i\sigma\hat{v}_k + 2\Omega\sin\varphi\hat{u}_k + \frac{1}{a}\frac{\partial\hat{\phi}_k}{\partial\varphi} = 0 \tag{2.3}$$

$$i\sigma\hat{T}_k - \frac{T_0}{\Delta p_k}(R_k\hat{\omega}_{k-1} + S_k\hat{\omega}_{k+1}) = -M_k\hat{T}_k \tag{2.4}$$

$$\hat{\phi}_k - \hat{\phi}_{k+2} = c_p(P_k\hat{T}_k + Q_{k+2}\hat{T}_{k+2}) \tag{2.5}$$

$$is\hat{u}_k + \frac{\partial}{\partial\varphi}(\hat{v}_k\cos\varphi) + a\cos\varphi(\hat{\omega}_{k+1} - \hat{\omega}_{k-1})/\Delta p_k = 0 \tag{2.6}$$

where any variable, say ψ, has been assumed a solution of the form,

$$\psi = \mathrm{Re}(\hat{\psi}e^{i(s\lambda+\sigma t)}) \tag{2.7}$$

s is the longitudinal wavenumber and σ is the angular frequency. Re ( ) is an operation to take a real part of ( ). Here s is assumed to be positive. Then a positive (negative) σ represents a westward (eastward) moving wave. The form of the vertical differencing of the first law of thermodynamics (2.4), and the hydrostatic equation (2.5) is just a linearized version of (1.11) and (1.18). We have included a damping term in (2.4), with the coefficient M_k, for later convenience. The coefficients R_k, S_k, P_k, and Q_k are given the following forms;

$$R_k=\frac{1}{T_o}\left(\frac{p_k}{p_o}\right)^{\kappa}(\bar{\theta}_{k-1}-\bar{\theta}_k) \tag{2.8}$$

$$S_k=\frac{1}{T_o}\left(\frac{p_k}{p_o}\right)^{\kappa}(\bar{\theta}_k-\bar{\theta}_{k+1}) \tag{2.9}$$

$$P_k=\left(\frac{p_o}{p_k}\right)^{\kappa}\ \left[\left(\frac{p_{k+2}}{p_o}\right)^{\kappa}-\left(\frac{p_k}{p_o}\right)^{\kappa}\right]\ \frac{\partial\bar{\hat{\theta}}_{k+1}}{\partial\bar{\theta}_k} \tag{2.10}$$

$$Q_{k+2}=\left(\frac{p_o}{p_{k+2}}\right)^{\kappa}\ \left[\left(\frac{p_{k+2}}{p_o}\right)^{\kappa}-\left(\frac{p_k}{p_o}\right)^{\kappa}\right]\ \frac{\partial\bar{\hat{\theta}}_{k+1}}{\partial\bar{\theta}_{k+2}} \tag{2.11}$$

where the overbar denotes the basic state. From the definition of $\hat{\theta}_{k+1}$, these coefficients for the isothermal basic state become

$$\begin{aligned}P_k=S_k&=\frac{(p_{k+2}/p_k)^{\kappa}-1-\ln(p_{k+2}/p_k)^{\kappa}}{(p_{k+2}/p_k)^{\kappa}-1}\\ Q_k=R_k&=\frac{(p_{k-2}/p_k)^{\kappa}-1-\ln(p_{k-2}/p_k)^{\kappa}}{1-(p_{k-2}/p_k)^{\kappa}}\end{aligned} \tag{2.12}$$

Eliminating $\hat{u}$ and $\hat{v}$ from (2.2), (2.3) and (2.6), we obtain

$$L(i\sigma\hat{\phi}_k)=4a^2\Omega^2\frac{\hat{\omega}_{k+1}-\hat{\omega}_{k-1}}{\Delta p_k} \tag{2.13}$$

where the differential operator L is given by

$$L=-\frac{\partial}{\partial\mu}\left(\frac{1-\mu^2}{f^2-\mu^2}\frac{\partial}{\partial\mu}\right)+\frac{1}{f^2-\mu^2}\left(\frac{s}{f}\frac{f^2+\mu^2}{f^2-\mu^2}+\frac{s^2}{1-\mu^2}\right) \tag{2.14}$$

where $\mu=\sin\varphi$ and $f=\sigma/2\Omega$.

From (2.4) and (2.5), on the other hand, we obtain

$$i\sigma(\hat{\phi}_k-\hat{\phi}_{k+2})=c_pT_o\ \left[\frac{S_k}{\xi_k\Delta p_k}(Q_k\hat{\omega}_{k-1}+S_k\hat{\omega}_{k+1})+\frac{Q_{k+2}}{\xi_{k+2}\Delta p_{k+2}}(Q_{k+2}\hat{\omega}_{k+1}+S_{k+2}\hat{\omega}_{k+3})\right] \tag{2.15}$$

Here

$$\xi_k=1-iM_k/\sigma.$$

Eliminating $\hat{\phi}_k$ between (2.13) and (2.15), we obtain

$$\frac{W_{k-1}-W_{k+1}}{\Delta p_k}-\frac{W_{k+1}-W_{k+3}}{\Delta p_{k+2}}=-\frac{c_pT_o}{gh}\ \left[\frac{S_k}{\xi_k\Delta p_k}(Q_kW_{k-1}+S_kW_{k+1})+\frac{Q_{k+2}}{\xi_{k+2}\Delta p_{k+2}}(Q_{k+2}W_{k+1}+S_{k+2}W_{k+3})\right] \tag{2.16}$$

where the separation of variable $\hat{\omega}_{k+1}=F(\mu)W_{k+1}$ and the separation constant, h, defined by

$$LF=\epsilon F,\ \epsilon=(2\Omega a)^2/gh \tag{2.17}$$

have been used. h and ϵ are often called equivalent depth and Lamb's parameter, respectively. (2.16) is a finite difference analog of the vertical structure equation. Let's assume, to this equation, the following solution,

$$W_{k+1}=\left(\frac{p_{k+1}}{p_o}\right)^{\alpha} \tag{2.18}$$

Setting $\xi_k=\xi_{k+2}=1$ in (2.16), we obtain two solutions for α, i. e., α_1 and α_2 ($=\alpha_1^*$: complex conjugate of α_1). The thick solid lines in Fig. 2.1 show Re (α_1) and $-$Im (α_1) $=$n as a function of ϵ. $d=\ln(p_{k+1}/p_{k-1})=0.658$ (or $e^d=1.93$) and $T_0=270°K$ are used in the calculation. The real part is 1/2, exactly as it is in the continuous case. There are some unavoidable errors in n, however, as n approaches the highest resolvable wavenumber π/d. The vertical wavelength ($=2\pi RT_0/gn$), therefore, tends to take a larger value in the discrete model, compared to that in the continuous case, with the increase of ϵ. At $\epsilon\simeq 2.1\times 10^4$, n is equal to π/d. Beyond that value, n remains equal to π/d, while Re (α_1) is no longer equal to 1/2, and damped and amplified oscillations occur. We cannot avoid these oscillations in the present discrete model, although the present vertical differencing scheme is superior to others as is discussed by Tokioka (1978).

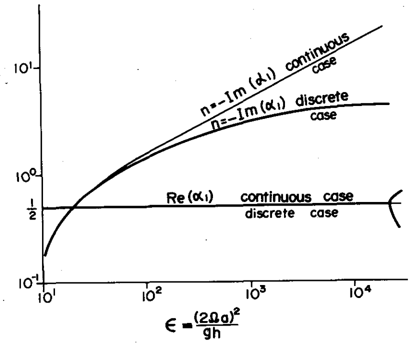

Fig. 2.1 The dependence of α (see Eq. (2.18)) on Lamb's parameter ϵ in an isothermal atmosphere (270°K) for both continuous case (thin line) and discrete case (thick line) where $d=\ln(p_{k+1}/p_{k-1})=0.658$. The vertical spacing of the MRI・GCM-I in the stratosphere (see Fig. 1. 2 (b)) is chosen to be d=0.658.

2.3 Effect of the upper boundary

Here we demonstrate the effect of an upper boundary condition $\omega=0$, which drastically alters the solution by thorough reflection of the wave energy and consequent resonance.

The solution of (2.16) is given by

$$W=A\left(\frac{p}{p_o}\right)^{\alpha_1}+B\left(\frac{p}{p_o}\right)^{\alpha_2}$$

If we confine our discussion to the westward moving waves ($\sigma>0$), the first term is responsible for upward propagation of wave energy and the second term is responsible for downward propagation of wave energy. For eastward moving waves, the situation is reversed. In the following we will consider a westward moving wave as an example.

Suppose that a wave is forced from below and that its energy propagates upwards. If the upper boundary condition is such that the wave energy can radiate away through the boundary (the radiation condition), there is no downward propagation of wave energy and we have the case $B=0$. Let us choose $A=1$ for convenience. This case, with $A=1$ and $B=0$, is considered to be the exact solution in the following discussion.

If the upper boundary condition is $\omega=0$, as in most numerical models, the solution is drastically altered. The boundary conditions then become

$$W=1 \quad \text{at} \quad p=p_0,$$
$$W=0 \quad \text{at} \quad p=p_t.$$

The coefficients A and B are now complex. Fig. 2.2 shows the real and imaginary parts of A and B, as a function of ϵ when $p_T=1\text{mb}$, $p_0=100\text{mb}$, $d=\ln\,(p_{k+1}/p_{k-1})=0.658$ and $T_0=270°\text{K}$. The real part of A has decreased from 1 to 1/2, and the real part of B has increased from 0 to 1/2. The imaginary parts of A and B become infinite when $-n\,\ln\,(p_t/p_o)=\pi,\ 2\pi,\ 3\pi,\cdots\cdots$. For these values of n, there exist free solutions of the vertical structure equation, which satisfy $\omega=0$ both at $p=p_0$ and $p=p_T$. With non-zero values of ω at $p=p_o$, a resonance occurs for discrete values of ϵ which give those values of n. Essentially the same result has been demonstrated by Lindzen *et al.* (1966).

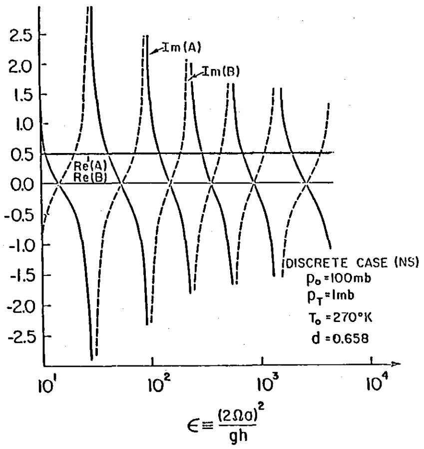

Fig. 2.2 The amplitude of the upward (A) and the downward (B) propagating modes as a function of ϵ, where the upper boundary condition $\dot{\sigma}=0$ is applied at $p=p_t=1\text{mb}$, and the wave is forced at $p=p_0=100\text{mb}$ in terms of vertical velocity. Isothermal atmosphere (270°K) is assumed with $d=0.658$.

2.4 Sponge layer formulation

2.4.1 Basic formulation

We now let the uppermost layer of the model be the sponge layer. Then $\xi_k=\xi=1-iM/\sigma$ for $k=1$, and $\xi_k=1$ for all other k. Let's again consider the isothermal case. The discrete vertical structure equation (2.16) at $k=2$, with the upper boundary condition $W_0=0$, is written as;

$$-e^{d}W_2-(W_2-W_4)=-\frac{c_pT_0}{gh}\left(e^{d}\frac{S^2}{\xi}W_2+Q(QW_2+SW_4)\right). \tag{2.19}$$

The vertical structure equations at other levels are written as;

$$e^{d}(W_{k-1}-W_{k+1})-(W_{k+1}-W_{k+3})=-\frac{c_pT_0}{gh}\left[e^{d}S(QW_{k-1}+SW_{k+1})+Q(QW_{k+1}+SW_{k+3})\right] \tag{2.20}$$

where

$$Q_k=Q=(e^{-\kappa d}-1+\kappa d)/(1-e^{-\kappa d})$$

$$S_k=S=(e^{\kappa d}-1-\kappa d)/(e^{\kappa d}-1).$$

By choosing ξ properly in (2.19), we can let the ratio W_4/W_2 be equal to that of the exact solution in the discrete model under the radiation condition, which is determined by (2.20) for a given equivalent depth. In this way, we can simulate a solution under the radiation condition. The resultant condition is

$$\epsilon\left(\frac{1-\xi}{\xi}X+\frac{Q}{S}\right)-\frac{(2\Omega a)^2}{c_pT_0S^2}=0 \tag{2.21}$$

X $(=W_4/W_2)$ in the above equation is determined by

$$\left[\epsilon+\frac{(2\Omega a)^2}{c_pT_0SQ}\right]X^2-\left[\frac{(2\Omega a)^2}{c_pT_0SQ}(e^{d}+1)-\epsilon\left(e^{d}\frac{S}{Q}+\frac{Q}{S}\right)\right]X+e^{d}\left[\epsilon+\frac{(2\Omega a)^2}{c_pT_0SQ}\right]=0 \tag{2.22}$$

One of the solutions of (2.22), which describes the structure of the upward energy propagating mode, should be substituted into (2.21). The upward energy propagating mode can be selected by the condition $n/\sigma<0$ *i. e.*,

$$\mathrm{Im}(X)\cdot\sigma<0 \tag{2.23}$$

Fig. 2.3 shows M/σ, thus obtained, as a function of $\epsilon=(2\Omega a)^2/gh$ when $T_0=270^\circ K$ and $d=0.658$. The required coefficient of the sponge term, M, is a complex function of the equivalent depth and frequency. The real part of M thus obtained remains

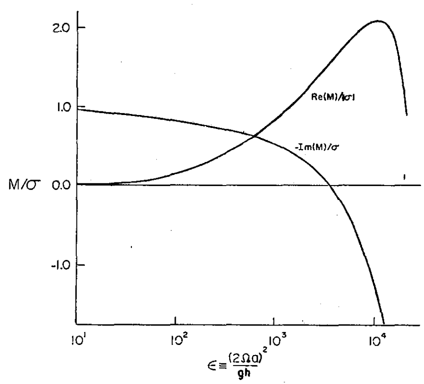

Fig. 2.3 Sponge coefficient M, normalized with frequency of a wave σ, as a function of Lamb's parameter ϵ. Conditions of the discrete model are the same as those in Fig. 2. 1.

positive while the wave is treated as internal (*i. e.*, $9.7<\epsilon<2.1\text{x}10^4$), and therefore acts as damping in that range. Beyond the value $\epsilon=2.1\text{x}10^4$, damped and amplified oscillations occur, as shown in Fig. 2.1. Therefore, proper simulation of wave in that range itself is meaningless. When ϵ is small ($\epsilon \lesssim 30$), Re (M)/ | σ | is quite small, while $-$Im (M)/σ is close to unity. This means that the sponge term has negligible damping effect but has exclusive effect in modifying vertical wavelength. With the increase of ϵ (or decrease of equivalent depth), the damping effect of the sponge term increases. At $\epsilon \simeq 3.5\text{x}10^3$, Im (M) vanishes, *i. e.* the sponge term formally reduces to the so called Newtonian cooling term.

Because the vertical wavelength of a wave is a decreasing function of ϵ, we may summarize the present result as follows; The sponge term is more effective in changing the vertical wavelength in the sponge layer than in damping the amplitude of the wave, for the waves with large vertical wavelengths. On the other hand, the damping effect of the sponge term becomes important to handle waves with short vertical wavelengths.

2.4.2 Estimation of equivalent depth and frequency

As mentioned in 2.4.1, the sponge coefficient M is a complex function of equivalent depth and frequency, both of which are not explicitly known in a numerical model. This causes difficulties in evaluating M in initial value problems.

In the following, we describe one successful way of estimating equivalent depth and frequency in a numerical model.

From (2.4), (2.5), (2.15) and (2.17), we have;

$$i\sigma\hat{T}_3-\frac{T_0}{\Delta p_3}(Q\hat{\omega}_2+S\hat{\omega}_4)=0 \tag{2.24}$$

$$\hat{\phi}_1-\hat{\phi}_3=c_p(S\hat{T}_1+Q\hat{T}_3) \tag{2.25}$$

$$i\sigma\hat{\phi}_1=gh\frac{\hat{\omega}_2}{\Delta p_1} \tag{2.26}$$

$$i\sigma\hat{\phi}_3=gh\frac{\hat{\omega}_4-\hat{\omega}_2}{\Delta p_3} \tag{2.27}$$

From (2.24) and (2.27), we obtain

$$gh=\frac{(2\Omega a)^2}{\epsilon}=\mathrm{Re}\Big(T_0\cdot\frac{Q+S\hat{\omega}_4/\hat{\omega}_2}{\hat{\omega}_4/\hat{\omega}_2-1}\frac{\hat{\phi}_3}{\hat{T}_3}\Big). \tag{2.28}$$

By knowing $\hat{\omega}_4/\hat{\omega}_2$ and $\hat{\phi}_3/\hat{T}_3$, ϵ can be estimated by (2.28). (2.24), (2.26) and (2.27) can be used to estimate σ. Once we know ϵ and σ, X is determined by (2.22) and (2.23). Finally, (2.21) gives us M.

2.4.3 Extension of the sponge layer model to the non-isothermal case with a constant zonal wind

We may extend the sponge layer formulation in the previous sub-section to the non-isothermal case with a constant zonal wind. We may include the effect of a constant wind by replacing σ with the doppler shifted frequency $\sigma^*(=\sigma+s\bar{u}/a\ \cos\varphi)$. The thermodynamic equation (2.4) should be replaced by

$$i\sigma^*\hat{T}_k-\frac{\bar{T}_k}{\Delta p_k}(R_k\hat{\omega}_{k-1}+S_k\hat{\omega}_{k+1})=-M_k\hat{T}_k-\hat{q}_k \tag{2.29}$$

where $\bar{T}_k$ is the globally averaged temperature at the level k, and $\hat{q}_k$ is the cooling rate due to diabatic processes other than the sponge term. T_o that appears in the definition of R_k and S_k should be replaced by $\bar{T}_k$.

The vertical structure equation is now written as follows;

$$\frac{W_{k-1}-W_{k+1}}{\Delta p_k}-\frac{W_{k+1}-W_{k+3}}{\Delta p_{k+2}}=-\frac{c_pT_o}{gh}\left[\frac{\bar{T}_k}{T_o}\frac{P_k}{\xi_k{}^*\Delta p_k}(R_kW_{k-1}+S_kW_{k+1})+\frac{\bar{T}_{k+2}}{T_o}\frac{Q_{k+2}}{\xi_{k+2}{}^*\Delta p_{k+2}}(R_{k+2}W_{k+1}+S_{k+2}W_{k+3})\right] \tag{2.30}$$

where

$$\xi_k{}^*=\xi_k+\hat{q}_k/i\sigma^*\hat{T}_k \tag{2.31}$$

In the following is given one practical way of evaluating sponge terms currently adopted. In order to evaluate them, we have to know both the equivalent depth and the doppler shifted frequency. For this end we estimate, at first, the vertical structure X $(=\hat{\omega}_{k+2}/\hat{\omega}_k)$ as follows;

$$X_{f.g.}=\frac{1}{3}\left\{\frac{\hat{\omega}_4}{\hat{\omega}_2}+\frac{\Delta p_5}{\Delta p_3}\left(\frac{\hat{\phi}_5}{\hat{\phi}_3}+\frac{\bar{T}_3}{\bar{T}_5}\cdot\frac{\xi_5{}^*}{\xi_3{}^*}\frac{\hat{T}_5}{\hat{T}_3}\right)\right\} \tag{2.32}$$

The doppler shifted frequency, σ^*, is estimated by use of (2.29). In doing so, a kind of time averaging is necessary to avoid a rapid fluctuation of the estimated value due to short lived waves. Currently the following form is adopted;

$$(\sigma^*)^\tau=(1-\varepsilon)(\sigma^*)^{\tau-1}+\frac{\epsilon}{2}\mathrm{Im}\ \left[\frac{1}{\Delta p_3}\cdot\frac{\bar{T}_3}{\hat{T}_3}(R_3\hat{\omega}_2+S_3\hat{\omega}_4)-\frac{\hat{q}_3}{\hat{T}_3}+\frac{1}{\Delta p_5}\frac{\bar{T}_5}{\hat{T}_5}(R_5\hat{\omega}_4+S_5\hat{\omega}_6)-\frac{\hat{q}_5}{\hat{T}_5}\right] \tag{2.33}$$

The averaging factor ε is assigned the value 0.08. Superscript τ indicates a time step to evaluate a sponge term. Currently this is done in every 60 min. The equivalent depth is estimated, now, with the use of a similar equation to (2.33), as follows;

$$(gh)^{\tau}=(1-\varepsilon)(gh)^{\tau-1}+\frac{\varepsilon}{2}\mathrm{Re}\left[\left(\frac{\bar{T}_3\hat{\phi}_3}{\xi_3{}^*\hat{T}_3}+\frac{\bar{T}_5\hat{\phi}_5}{\xi_5{}^*\hat{T}_5}\right)\cdot\frac{\bar{S}X_{f.g.}+\bar{R}}{X_{f.g.}-1}\right] \tag{2.34}$$

where $\bar{S}$ and $\bar{R}$ are representative values of S_k and R_k in the highest three levels. ε is again set to 0.08.

We are now able to recalculate the vertical structure X by use of the vertical structure equation (2.30) applied at the level $k=4$. This gives us two solutions for X, *i. e.*, X_1 and X_2. We choose X_1 when X_1 satisfies either

$$\begin{aligned} &|X_1| > |X_2| \\ &\text{or} \qquad\qquad\qquad\qquad\qquad\qquad\qquad (2.35)\\ &|X_1| = |X_2| \quad \text{and} \quad \mathrm{Im}(X_1)\sigma^* < \mathrm{Im}(X_2)\sigma^* \end{aligned}$$

The sponge coefficient M is determined by use of the vertical structure X_1 thus determined and the vertical structure equation applied at the level $k=2$. Currently, sponge terms are calculated for each latitude circle for the zonal wavenumber up to 4.

A2.1 Test examples of the sponge layer model

A2.1.1. Model

We apply the sponge layer model designed in 2.4 to the linearized equatorial β-plane model. We assume rest, isothermal atmosphere as a basic state and consider the following form of a perturbation motion,

$$\begin{pmatrix} u \\ v \\ \omega \\ T \\ \phi \end{pmatrix} = \mathrm{Re}\begin{pmatrix} \tilde{u} \\ \tilde{v} \\ \tilde{\omega} \\ \tilde{T} \\ \tilde{\phi} \end{pmatrix}\cdot e^{imx}$$

where m is a wavenumber in the zonal direction. Then we obtain a following set of linearized equations;

$$\delta_t\tilde{u}_j-\frac{1}{2}f_j(\tilde{v}_{j+1}+\tilde{v}_{j-1})=-im\tilde{\phi}_j \tag{A2.1.1}$$

$$\delta_t\tilde{v}_j+\frac{1}{2}(f_{j+1}\tilde{u}_{j+1}+f_{j-1}\tilde{u}_{j-1})=-\frac{1}{\Delta y}(\tilde{\phi}_{j+1}-\tilde{\phi}_j) \tag{A2.1.2}$$

$$\delta_t\tilde{T}_k-\frac{T_0}{\Delta p_k}(Q\tilde{\omega}_{k-1}+S\tilde{\omega}_{k+1})=-M_k\tilde{T}_k \tag{A2.1.3}$$

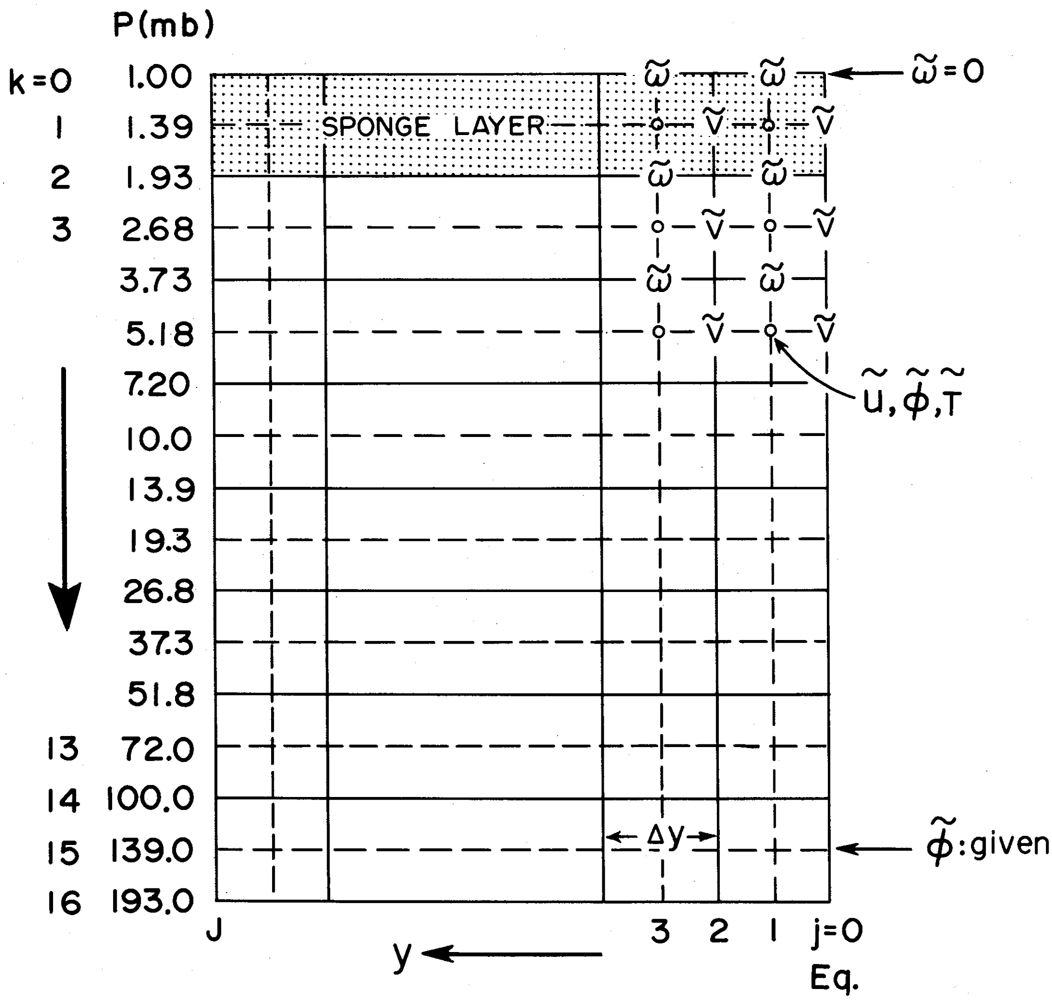

Fig. A2.1.1 The vertical and the horizontal structure of the discrete model used for the test calculations. Vertical structure is the same as that in Fig. 1.2(b).

$$\tilde{\phi}_k - \tilde{\phi}_{k+2} = c_p(S\tilde{T}_k + Q\tilde{T}_{k+2}) \tag{A2.1.4}$$

$$im\tilde{u}_j{}^k + \frac{1}{\Delta y}(\tilde{v}^k{}_{j+1} - \tilde{v}^k{}_{j-1}) + \frac{1}{\Delta p_k}(\tilde{\omega}_j{}^{k+1} - \tilde{\omega}_j{}^{k-1}) = 0 \tag{A2.1.5}$$

where

$$f_j = \frac{j}{2}\Delta y \frac{2\Omega}{a}$$

M_k is set to zero except the one at $k=1$, which is estimated by the procedure described in section 2.4. Location of variables is shown in Fig. A2.1.1. Horizontal location of variables corresponds to the scheme adopted by the MRI • GCM-I. Q and S in (A2.1.3) and (A2.1.4) are

Table A2.1.1

Numerical parameters and lateral boundary conditions used in initial value problems. Δy is a grid size in the meridional direction, J the number of grids in y-direction, Δt a time increment, and m a wavenumber in the longitudinal direction.

Case	Δy(km),J	Δt(sec)	m(M^{-1})	Lateral Boundary Condition	Assigned Frequency (sec^{-1})	$\varepsilon=\frac{(2\Omega a)^2}{gh}$
Mixed Rossby-Gravity Wave	444.78 (J=22)	450.	6.2784×10^{-7}	$\tilde{u}_1=\tilde{u}_{-1}$ $\tilde{v}_J=0$	6.2784×10^{-6}	2.030×10^{3}
Kelvin Wave	444.78 (J=22)	450.	1.5696×10^{-7}	$\tilde{v}_O=0$ $\tilde{v}_J=0$	-6.0602×10^{-5}	5.760×10^{3}
Rossby Wave	600. (J=22)	600.	3.1392×10^{-7}	$\tilde{v}_O=0$ $\tilde{v}_J=0$	8.0×10^{-6}	1.230×10^{2}
Semi-Dirunal Wave	600. (J=21)	600.	3.1392×10^{-7}	$\tilde{v}_O=0$ $\tilde{\phi}_J=0$	1.4526×10^{-4}	1.219×10^{1}

the ones defined in (2.12). Vertical index k and latitudinal index j are dropped in the momentum equations, and in the thermodynamic and hydrostatic equations, respectively. As for the time differencing, δ_t, we use the centered scheme with a periodical insertion of the Euler backward step.

By use of the separation relation;

$$\frac{1}{\Delta p_k}(\tilde{\omega}_{k+1}-\tilde{\omega}_{k-1})=\frac{i\sigma}{gh}\tilde{\phi}_k \tag{A2.1.6}$$

and (A2.1.1), (A2.1.2) and (A2.1.5), a difference analog of the horizontal structure equation is obtained. The equivalent depth, or Lamb's parameter, and the eigenfunction for geopotential, **F**, are obtained by solving it under the lateral boundary conditions listed in Table A2.1.1. The eigenfunction thus obtained is used as the forcing to the model. Geopotential at the lowest level (k=15) is prescribed as

$$\tilde{\phi}_j^{15}=\Phi\mathbf{F}\,e^{i\sigma\Delta t\tau} \tag{A2.1.7}$$

where τ is a time step, and Φ is a constant chosen to be $|\phi_{j=1}^{15}|=10.0m^2sec^{-2}$. Prescribed frequency σ is not used in any other places than in (A2.1.7), in the model. Integrations are started from a rest condition in the interior.

Four examples of the initial value problem are demonstrated in the following. They are the propagation of a mixed Rossby-gravity wave, a Kelvin wave, a Rossby wave and a semi-diurnal wave (see Table A2.1.1). Lamb's parameter ϵ are chosen in such a way as to be close to the resonance points except a semi-diurnal wave case. Arrows in Fig. A2.1.2 show the location of Lamb's parameters listed in Table A2.1.1. The differences between Fig. 2.2 and A2.1.2 are due to the differences in the forcing level and the way in which waves are forced. In Fig. A2.1.2, waves are forced by ϕ at the level k=15, while they are forced by ω at the level k=14 in Fig. 2.2.

A2.1.2. Propagation of a mixed Rossby-gravity wave

As the first test, we simulate a propagation of a mixed Rossby-gravity wave. This is observed in the equatorial lower stratosphere. The parameter in Table A2.1.1 roughly simulates the observed waves.

The equivalent depth is $gh=424\text{m}^2\,\text{sec}^{-2}$ or $\epsilon=2.03\times10^3$. Therefore the vertical wavelength in the present discrete model is estimated approximately as 12.5km with the aid of Fig. 2.1. While the continuous model gives about 5km for the same value of ϵ. The horizontal profile of $\mathbf{F}$, used as the boundary forcing, is proportional to the one shown in Fig. A2.1.3 (c) by E.

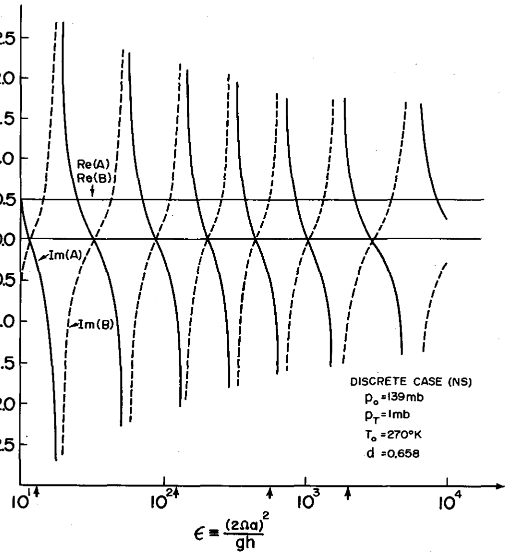

Fig. A2.1.2 Same as in Fig. 2.2 except that waves are forced at the level p=139mb in terms of geopotential. Arrows indicate positions of Lamb's parameter used as the forcing in the present test (see Table A2.1.1).

The time change of the amplitude of $\tilde{\phi}^3_{j=1}$ is shown in Fig. A2.1.3 (a), where the solid line with (S) is the case with the sponge layer, and the dashed line with (NS) is the case without the sponge layer. The thin solid line with (E) shows the steady state amplitude of the exact solution with the sponge layer, which is identical to the exact solution under the radiation condition below the sponge layer. We do not observe any significant differences between Cases (S) and (NS) until about 240 hours. However, the amplitude of (NS) still continues to increase and tends to have a large value after that. On the other hand, the amplitude of (S) fluctuates around the exact value.

The vertical structure at j=1 (Fig. A2.1.3 (b)) and the horizontal structure at k=3 (Fig. A2.1.3 (c)) of geopotential field show that the sponge layer well supresses artificial reflections,

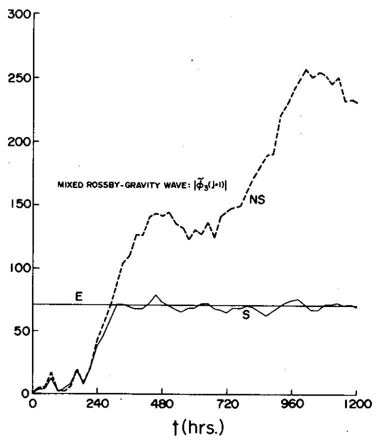

(a)

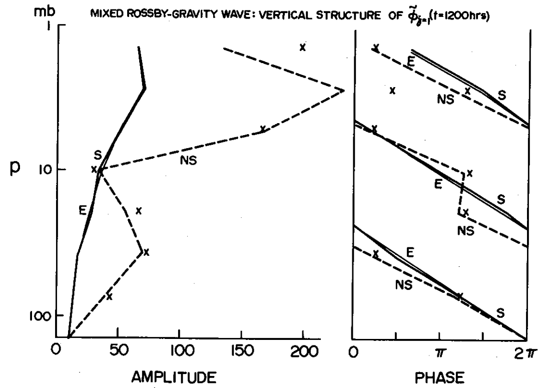

(b)

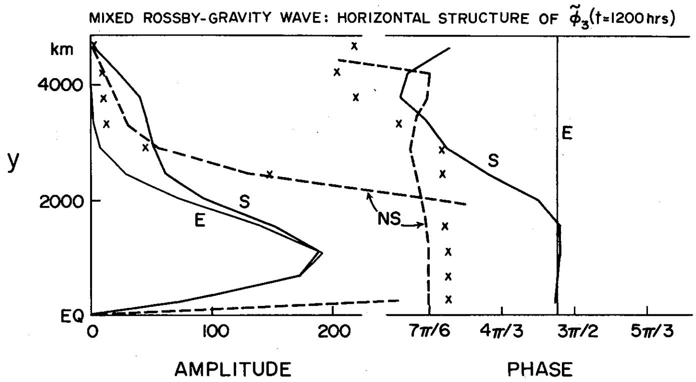

(c)

Fig. A2.1.3 (a) The time change of geopotential amplitude at the grid point $j=1$, $k=3$ for the mixed Rossby-gravity wave case (unit : $m^2.\ s^{-2}$). "S" and "NS" indicate the case with and without the sponge layer, respectively. "E" is the exact steady solution with the sponge. The exact solution is identical to the solution under the radiation condition, below the sponge layer.

(b) The vertical structure of geopotential at $j=1$ after 1200 hours of integration for the mixed Rossby-gravity case. Amplitude is shown in unit of $m^2.\ s^{-2}$. The phase is measured relative to that at the bottom layer ($k=15$). Crosses indicate the results where Rayleigh friction terms with the damping rate $10^{-5}s^{-1}$ are included in the momentum equations at the level $k=1$ as well as a Newtonian cooling term with a constant cooling rate 10^{-5} s^{-1} in the thermodynamic equation at $k=1$.

(c) The horizontal structure of geopotential at $k=3$ after 1200 hours of integration for the mixed Rossby-gravity case. Amplitude unit is $m^2.\ s.^{-2}$

caused by the upper boundary condition $\omega=0$, below the sponge layer. The solution below that layer is almost identical to the exact one, in this example. Vertical profile of $|\tilde{\phi}|$ in (NS) clearly shows the exisistence of a nodal point caused by reflections at the top.

When there is a Rayleigh friction term in the momentum equation, simple analysis of the effect of the term is prohibited because of the change in the horizontal structure between the layers with and without the Rayleigh friction term. Because the Rayleigh friction term is sometimes included in the model for the purpose of dissipating reflected waves caused by the upper boundary, the method is tested numerically.

In the numerical test, a Newtonian cooling term is also retained in the model with a constant cooling rate. Both the momentum damping rate and the cooling rate are set to 10^{-5} $\sec^{-1}$ and those damping terms are included only in the highest layer. Crosses in Fig. A2.1.3 (b) and (c) show the geopotential field after 1200 hrs. of integration. Gross features are very close to those without sponge (NS). The case with the damping rate of 10^{-6} $\sec^{-1}$ has also been tested. However, the change in the damping rate does not cause much differences in the results except in the highest three levels.

A2.1.3. Propagation of a Kelvin wave

Kelvin waves are also dominantly observed in the tropical lower stratosphere. The parameters in Table A2.1.1 roughly simulates observed Kelvin waves.

Because $\tilde{v}_j \equiv 0$ in the Kelvin wave, the dispersion relation reduces simply to

$$\sigma = -\sqrt{gh}\,m \tag{A2.1.8}$$

This gives us 1.49 x 10^3 m^2sec^{-2} as gh (or $\epsilon=576$). The vertical group velocity W_g of the Kelvin wave, in the present discrete model, can be evaluated with the aid of the following relation;

$$W_g = -H_0\frac{\partial\sigma}{\partial n} = \frac{H_0\sigma}{2}\cdot\frac{\partial \ln\epsilon}{\partial n} \tag{A2.1.9}$$

where H_0 is the equivalent depth $(=C_pT_0/g)$ and use has been made of (A2.1.8). $\partial \ln\epsilon/\partial n$ in the present model can be evaluated from Fig. 2.1. Thus we obtain 2km $\cdot$ d^{-1} as an approximate value of W_g for the present choice of parameters.

Fig. A2.1.4 (a) shows the time change of $|\tilde{\phi}^3{}_{j=1}|$. We notice a great difference between Cases (S) and (NS) after about 380 hrs. The value 380 hrs is compared well with the value 400 hrs, which is an approximate time required for the bottom disturbance to arrive at the level $k=3$.

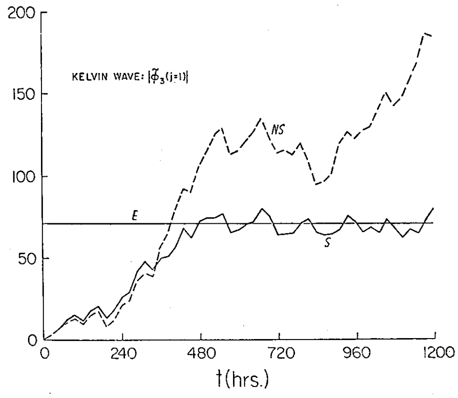

(a)

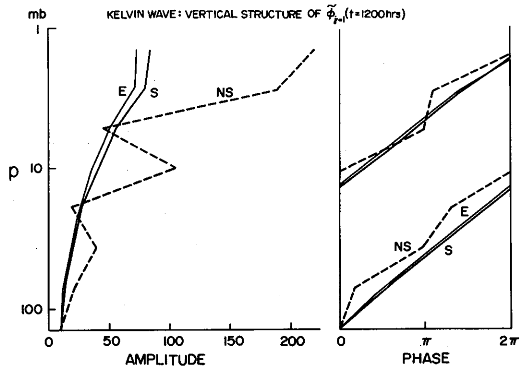

(b)

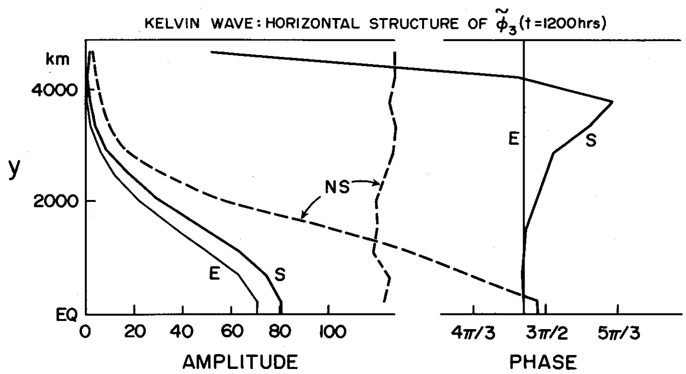

(c)

Fig. A2.1.4 Same as in Fig. A2.1.3 (a), (b) (c) except for the case with a Kelvin wave forcing (see Table A2.1.1).

After 400 hrs, the amplitude of the case with sponge (S) fluctuates around the exact value (E). While the amplitude of (NS) seems to settle at a large value. This is a plausible result because the Lamb's parameter ($\epsilon=576$) is close to a resonance point (see Fig. A2.1.2).

Vertical and horizontal structures of geopotential at 1200 hrs are shown in Fig. A2.1.4 (b) and (c). From those figures, again, we see that (S) is close to (E) except near the north boundary region where the amplitude of geopotential itself is small. We may conclude that the sponge layer is effective in this case.

A2.1.4. Propagation of a Rossby wave

The third example is a Rossby wave's case. The parameters in Table A2.1.1 are chosen so as to locate Lamb's parameter around 10^2. The value is about 123, and this value is also close to a resonance point (see Fig. A2.1.2).

The time change of geopotential amplitude at $j=1$ and $k=3$ is shown in Fig. A2.1.5 (a). The amplitude of (S) follows the exact value (E) more closely than that of (NS) after about 300hrs of integration. However, there still remains larger fluctuation in (S) around the exact value than those observed in the previous two cases.

Although we do not see much preference of (S) over (NS) from Fig. A2.1.5 (a) alone, the vertical structure in Fig. A2.1.5 (b) clearly reveals differences between (S) and (NS). Both amplitude and phase of geopotential in (S) are close to the exact values. On the other hand, we notice two sharp nodes in (NS). One of the nodes is located at the level $k=3$.

Judging from both Figs. A2.1.5 (b) and (c), we may say that not bad horizontal structure of geopotential in (NS) at a particular level $k=3$ (Fig. A2.1.5 (c)) has happened by chance.

A2.1.5. Propagation of a semi-diurnal wave

As the last example, we test a propagation of Θ (2,2) mode of the semi-diurnal tidal motion (see Chapman and Lindzen (1970) for further details). By use of the parameters in Table A2.1.1, the simulated Θ (2,2) mode in the present discrete model gives $gh=7.04 \times 10^4$ m^2sec^{-2} or $\epsilon=12.2$, which gives about 190km as the vertical wavelength.

Fig. A2.1.6 (a) shows the time change of geopotential amplitude at $j=1$, and $k=3$. Corresponding to the very large vertical wavelength, the vertical group velocity is also quite large. Within 12 hrs, wave energy arrives at the sponge layer. However, the amplitude of (S) does not converge to the exact one. There still remains a large fluctuation even after 1200 hrs, and no preference of (S) over (NS) is found both in the horizontal and vertical structures of

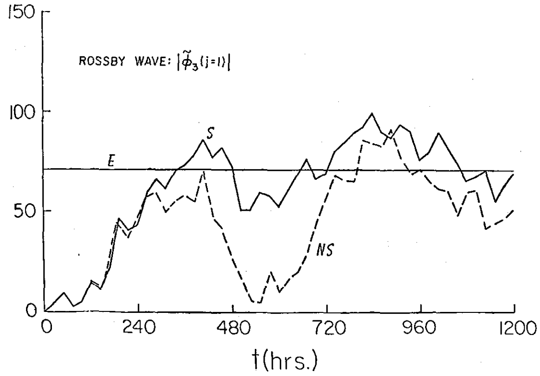

(a)

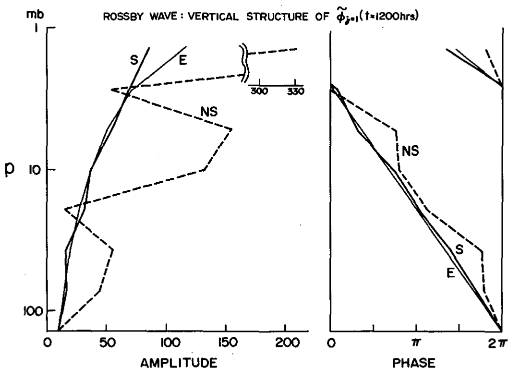

(b)

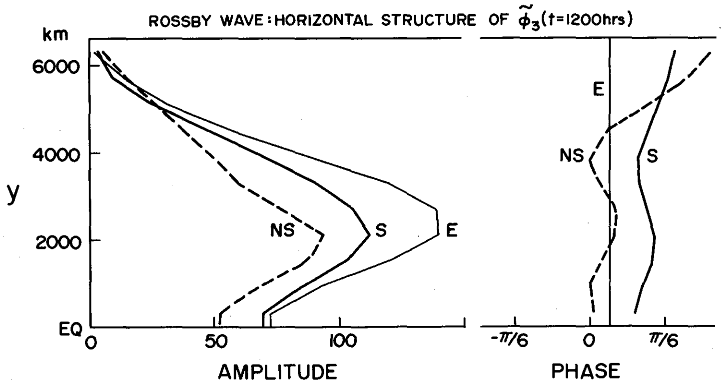

(c)

Fig. A2.1.5 Same as in Fig. A2.1.3 (a), (b) (c) except for the case with a Rossby wave forcing (see Table A2.1.1).

geopotential shown in Fig. A2.1.6 (b) and (c).

In the previous three cases, especially in the first two, the sponge layer was quite effective in supressing reflection of waves below the sponge layer. While, in the present case, it is not. One reason for the ineffective sponge in the present case may be explained as follows; Because we have assumed a steady state in designing the sponge layer model, there is no surprise even when the sponge did not work at the arrival of wave fronts. If the vertical group velocity is small, in vague sense, not much noise may be created at the arrival of the main wave front. On the other hand, if it is large, as is the case for the mode Θ (2,2), much noise might be created, which might cause the sponge model ineffective.

Another reason may be due to the small value of Re (M)/ $|\sigma|$ for the mode Θ (2,2) (see Fig. 2.3). Because there are no dissipative mechanisms other than the sponge term in the present linearized numerical model, secondary noise may not be supressed well by the sponge term alone.

One may point out, as one of the reasons for the ineffective sponge in the present case, the way in estimating the sponge term. It is estimated by use of the informations in the highest three levels, the depth of which is too thin compared to the vertical wavelength of Θ (2,2). We admit that the estimated value of M had not a small fluctuation around the expected value of it. However, we do not consider this as the major cause for the unsatisfactory results in the present case because the run where M was fixed to the exact value, expected in the steady state, did not show much improvement over (S).

A2.2 Stability check of Eq. (2.1) as an upper boundary condition

When we apply Eq. (2.1) as an upper boundary condition, we may rewrite it as follows,

$$\frac{\partial}{\partial t}\left(\frac{\omega}{\sqrt{p}}\right)+c\frac{\partial}{\partial p}\left(\frac{\omega}{\sqrt{p}}\right)=0 \qquad \text{(A2.2.1)}$$

We discuss in this appendix the stability characteristics of free modes when the use has been made of (A2.2.1) as an upper boundary condition.

Because c, in (A2.2.1), is to be chosen in such a way as to radiate vertically propagating wave energy outward, c must be a positive value.

Let's consider a rest, isothermal model in which there are no variations of variables in the north-south direction, and the Coriolis parameter f is constant. We assume the following form of a solution to the linearized system equations:

$$q_k=\mathrm{Re}(\hat{q}_k e^{i(\sigma t+mx)}) \qquad \text{(A2.2.2)}$$

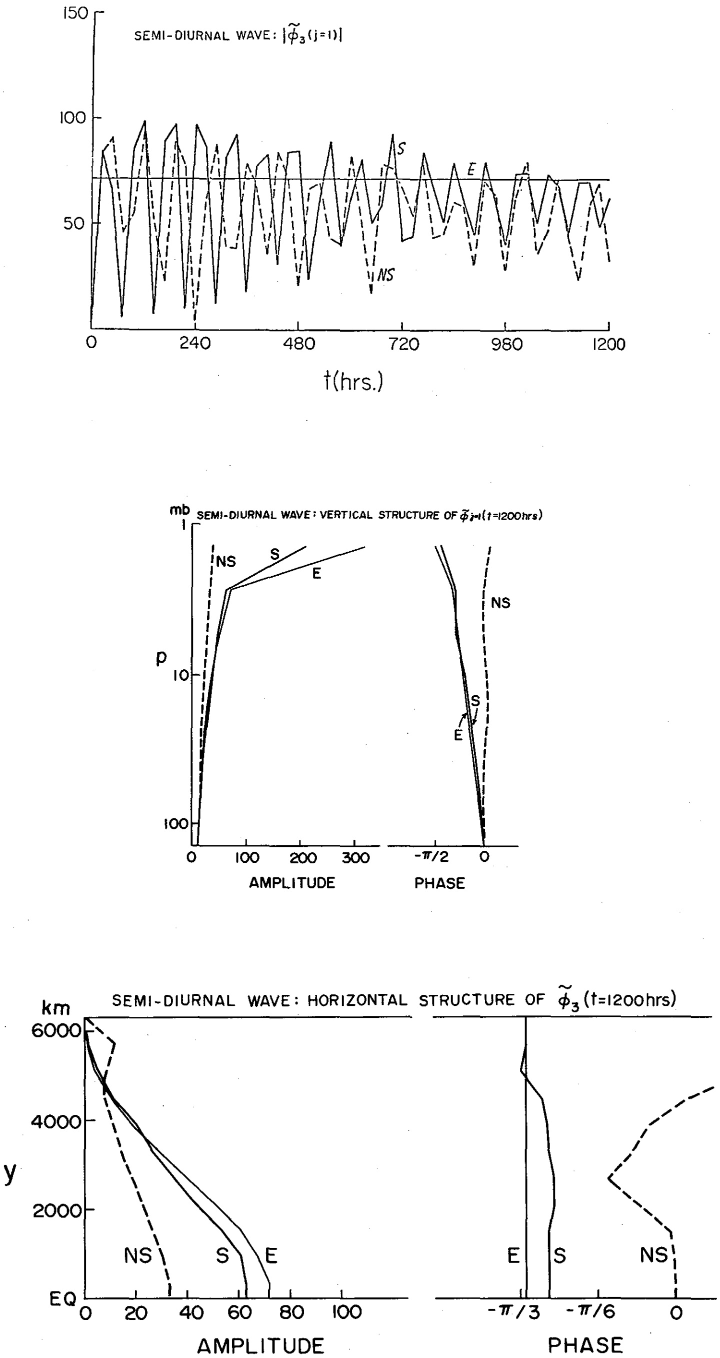

Fig. A2.1.6 Same as in Fig. A2.1.3 (a), (b) (c) except for the case with a semi-diural wave forcing (see Table A2.1.1).

We use the same notations as have been used in the text. Then, the linearized system of equations are written as follows:

$$i\sigma\hat{u}_k - f\hat{v}_k = -im\hat{\phi}_k, \tag{A2.2.3}$$

$$i\sigma\hat{v}_k + f\hat{u}_k = 0, \tag{A2.2.4}$$

$$i\sigma\hat{T}_k - \frac{T_o}{\Delta p_k}(S\hat{\omega}_{k+1} + Q\hat{\omega}_{k-1}) = 0, \tag{A2.2.5}$$

$$\hat{\phi}_k - \hat{\phi}_{k+2} = c_p(S\hat{T}_k + Q\hat{T}_{k+2}), \tag{A2.2.6}$$

$$im\hat{u}_k + \frac{1}{\Delta p_k}(\hat{\omega}_{k+1} - \hat{\omega}_{k-1}) = 0,\ (k=1,\ 3, \cdots\cdots,\ 2K-1). \tag{A2.2.7}$$

From these five equations, we obtain the following equation:

$$e^d A\hat{\omega}_{k-1} - B\hat{\omega}_{k+1} + A\hat{\omega}_{k+3} = 0, \tag{A2.2.8}$$

where

$$A = X^2 - c_p T_o m^2 QS - f^2,$$

$$B = (1+e^d)X^2 + c_p T_o m^2(e^d S^2 + Q^2) + (1+e^d)f^2,$$

$$X = i\sigma,$$

$$e^d = \Delta p_k / \Delta p_{k-2}$$

We apply the bottom boundary condition as

$$\hat{\omega}_{2K} = 0. \tag{A2.2.9}$$

As for the top boundary condition, we express (A2.2.1) in the following form,

$$X(\hat{\omega}_0 + e^{-\frac{d}{2}}\hat{\omega}_2) - \gamma(\hat{\omega}_0 - e^{-\frac{d}{2}}\hat{\omega}_2) = 0,$$

where $\gamma = 2c/\Delta p_1$. (A2.2.10)

Equations (A2.2.8), (A2.2.9) and (A2.2.10) determine eigen-value X. When we apply $\hat{\omega}_0 = 0$ instead of (A2.2.10) as the top boundary condition, all eigen solutions are neutral, of course, and there are no computational modes in the solutions.

If we use (A2.2.10) as the top boundary condition, instead, all inertio-gravity modes suffer slight damping (stabilization) for positive value of γ. In the present system,

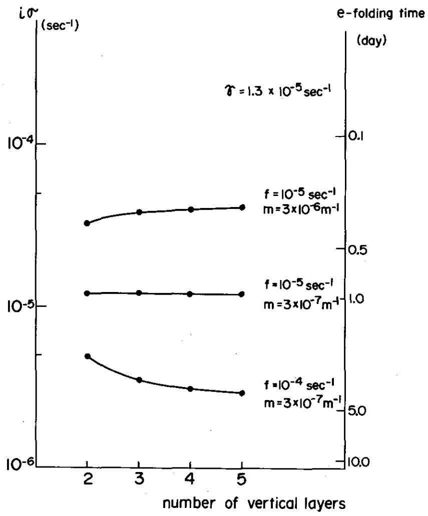

Fig. A2.2.1 The growth rate of the unstable mode as a function of the number of vertical layers, K, when Eq. (A2.2.1) is the upper boundary condition. f and m are the Coriolis parameter and the zonal wavenumber. The same vertical gridding as is shown in Fig. A2.1.1 is used. T_0 is set to 270°K.

however, we have one additional computational mode due to the use of (A2.2.10). This mode is unstable. The growth rate of the solution is shown in Fig. A2.2.1 for a particular value of γ. Numerical values used for the calculation are as follows:

$d=0.658$, $T_o=270K$, $c_p=1004m^2s^{-2}K^{-1}$, $S=9.1\times10^{-2}$,

$Q=9.7\times10^{-2}$, $\Delta p_1=1.93mb$ and $\gamma=1.3\times10^{-5}s^{-1}$.

The growth rate of the unstable mode does not change much with the increase of the number of the vertical layers K. We see that this mode becomes more unstable with the decrease of the Coriolis parameter f and with the increase of the zonal wavenumber m. To make the situation worse, the growth rate is quite large. The rapid growth of errors (about 1/4 day in e-folding time) was observed in the initial value problem test when Eq. (A2.2.1) was used as the upper boundary condition with the same Rossby wave forcing as listed in Table A2.1.1, in which γ is approximately equal to $1.3\times10^{-5}\ s^{-1}$.